Sensors and Actuators A 215 (2014) 36–43

Contents lists available at ScienceDirect

Sensors and Actuators A: Physical

journal homepage: www.elsevier.com/locate/sna

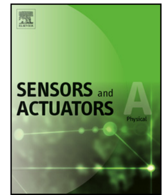

Metal-armouring for shock protection of MEMS☆

A.K. Delahunty*, W.T. Pike

Optical and Semiconductor Devices Group, Imperial College London, United Kingdom

ARTICLE INFO

Article history:
Received 15 April 2013
Received in revised form 5 November 2013
Accepted 9 November 2013
Available online 17 November 2013

Keywords:
MEMS
Shock protection
Metal-armour
Solder

ABSTRACT

This paper demonstrates a novel concept for the shock protection of MEMS suspensions: solder is incorporated within the sidewalls of the suspension to produce protective metal armouring. This provides solder–solder contact at the extremes of the suspension travel, greatly increasing the shock resistance. Model suspension systems were fabricated using deep reactive ion etching (DRIE) and shock tested in a drop-test rig at acceleration levels up to 6000 × g. The solder armour proved to absorb ∼90% of the collision kinetic energy and double the shock resistance of the MEMS suspension.

© 2013 Published by Elsevier B.V.

1. Introduction

With MEMS becoming increasingly commonplace in many different industries, the need for more robust microstructures that can withstand high shock environments is now more important than ever. Consumer electronics need to be able to reliably withstand accidental drops, sensors used in the automotive industry as well as MEMS being considered for Military applications [1] need to cope with severe in-use conditions and because of their easy integration with IC circuitry and their reduced mass and power consumption, MEMS are now being used for space applications where they are required to survive significant shock and vibration forces during both the launch and separation stages as well as during deployment and operation [2].

Current shock protection methods for MEMS include *external protection methods*: mechanical latching [3], electrostatic clamping [4], electromagnetic clamping [5] and encapsulating the devices in a wax which sublimes in the vacuum of space [6], or *internal protection methods*: optimising dimensions to withstand a known force [7] or using squeeze film damping [8], compliant non-linear springs [9,10], hard shock-stops [11], metal armouring [9], parylene coatings [10] or microglass beads [12] to dissipate energy. A shock absorber which is suitable for both space and terrestrial applications and which can absorb significant amounts of energy without needing a power source or without adversely affecting the performance of the device does not currently exist. This work presents a novel shock-protection method for MEMS which successfully satisfies these requirements.

2. Design concept

Providing a shock absorber which can absorb the energy of an impact is an effective method of increasing the robustness of a MEMS device. When designing shock protection the aim is to absorb the maximum amount of energy within a minimum amount of time, with energy generally being absorbed through the deformation of solids, either through plastic flow or controlled brittle fracture [13]. We propose using solder as a form of metal armouring to protect the silicon suspension during a shock event; replacing brittle silicon–silicon impact with ductile solder–solder impact. The solder should deform upon impact, absorbing large amounts of energy in the process and eliminating the risk of brittle silicon fractures.

Metal armouring was first proposed to mitigate shock damage by Yoon et al. [9]. Using softer materials at the point of impact, the number of collisions as well as the post-shock settling time is reduced. However the sidewall deposition of gold which they propose should reduce the impact forces, but such metallisation is not straightforward, and the limited thickness of metal constrains the protective potential. We have previously used solder reflow on metal pads to produce more substantial bumpers able to undergo significant plastic deformation. These are fabricated to overhang the collision points of the suspension (Fig. 1a). However although

☆ This is an open-access article distributed under the terms of the Creative Commons Attribution-NonCommercial-No Derivative Works License, which permits non-commercial use, distribution, and reproduction in any medium, provided the original author and source are credited.

* Corresponding author. Tel.: +44 (0)20 7594 6242.
E-mail addresses: a.delahunty09@imperial.ac.uk, aifricd@gmail.com (A.K. Delahunty).

0924-4247/$ – see front matter © 2013 Published by Elsevier B.V.
http://dx.doi.org/10.1016/j.sna.2013.11.008

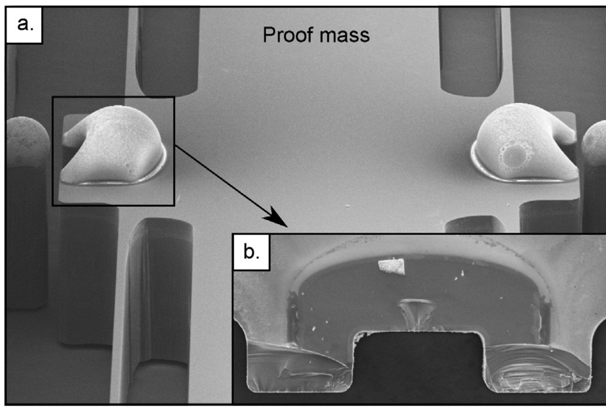

Fig. 1. (a) Bumpers created through the reflow of solder on metal pads (before shock testing), (b) solder bumper failed at the pad–wafer interface during a shock event. The damage at the silicon bumper tips occurred during rebound after the solder bumper de-adhered and was no longer available to protect the silicon.

enhancing the robustness, upon collision these bumpers can fail due to de-adhesion at the pad–wafer interface (Fig. 1b).

This work, originally reported here [14], avoids the limitations of both sidewall metallisation and pad-mounted bumpers: the solder is incorporated directly into the sidewall by reflow of solder balls in through-wafer conduits. The resulting bumpers collide at the centre of percussion of the suspension, and should absorb maximum energy from the fundamental mode of the suspension, and minimise the excitation of cross-axis modes.

3. Fabrication

3.1. Silicon suspension systems

Model suspensions, consisting of folded cantilevers either side of a proof mass, were fabricated using through-wafer deep reactive ion etching (DRIE) (Fig. 2a). High quality vertical side-walls are achieved by using a Halo mask [15,16] to minimise the effects of both microloading [17] and etch lag [18] and a thin sacrificial aluminium layer is deposited on the back side of the wafer using a thermal evaporator to prevent notching at the foot of the microstructure [19]. The aluminium provides a conductive layer which eliminates charge build up towards the end of the etch, otherwise a positively charged insulator surface will deflect the ions towards the sidewall resulting in a lateral etch. Once etching is complete the aluminium layer is stripped.

3.2. Solder bumpers

The collision points at the centre of the suspension incorporate conduits that can accommodate two solder balls (Fig. 2b) which reflow to form the bumpers which are mechanically keyed in place (Fig. 2c): two 300 μm-diameter $Sn_{3.0}Ag_{0.5}Cu$ solder balls reflow to form bumpers in a 500 μm-thick wafer. The solder balls are lightly dipped in flux before being placed in the through-wafer conduits. The flux helps (a) to keep the solder balls in place before reflow and (b) to promote reflow between the two balls. A solder rig with a conductive heating stage and a sealed chamber is used for reflow. Nitrogen gas is used to purge air in the sealed chamber prior to heating, and the stage is heated to a peak temperature of 260 °C, remaining above the melting temperature of the solder (220 °C) for a minimum of 5 min.

4. Bumper design

4.1. Conduit geometry

The final reflow profile of the solder was simulated using Surface Evolver [20], which uses finite element analysis (FEA) to calculate the equilibrium shape of the molten solder subject to relevant constraints and forces; namely surface tension, gravity, the geometric

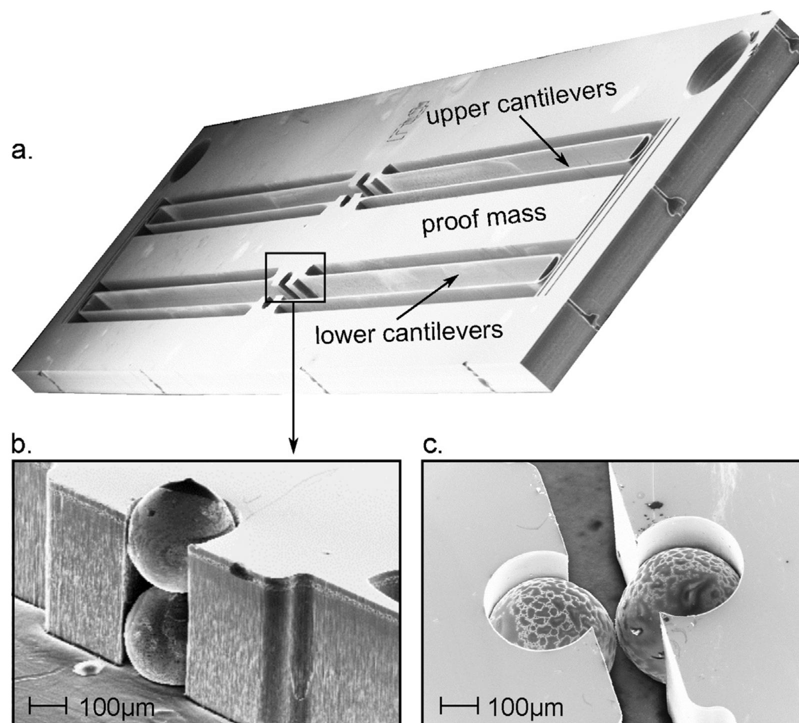

Fig. 2. (a) Model suspension system, (b) solder balls before reflow, and (c) solder bumper after reflow.

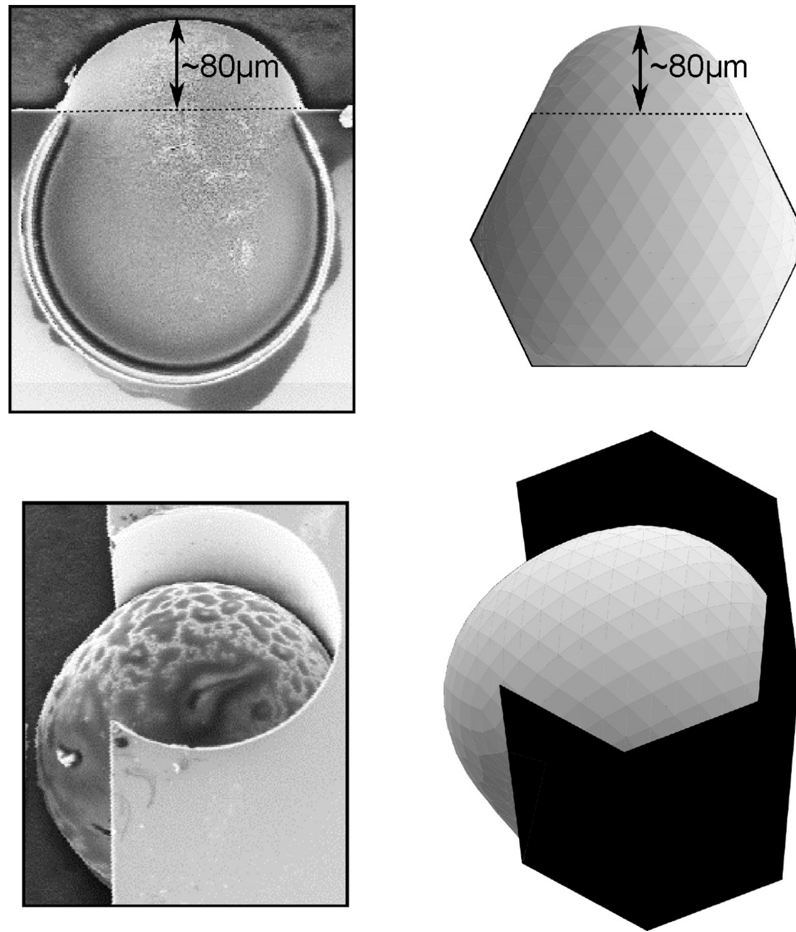

Fig. 3. Surface Evolver simulations of the solder bumpers (plan and side views) are compared to actual fabricated devices. The geometry of the exposed solder correlates well.

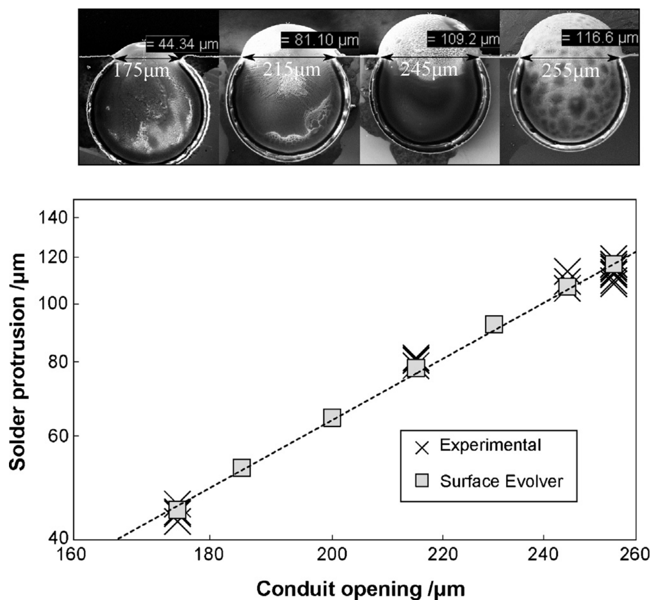

Fig. 4. The experimental results for the solder protrusions (measured from SEM images) correlate well with Surface Evolver simulations. Good repeatability for the production of the solder protrusion is also evident.

constraints of the conduit and the volumetric constraints of the solder. For ease of analysis the circular conduit was modelled as a hexagon (Fig. 3); this allows easier definition of the geometric constraints.

The depth of the solder protrusion proud of the silicon is governed surface tension and set by the width of the conduit opening. As the opening width increases so too does the volume of solder exposed. The simulated results correlate extremely well with the observed experimental results (Fig. 4). Plotting the results on a log–log scale the depth of the solder protrusion in relation to the conduit opening follows a distinct power law. Good repeatability of the final reflow profiles of solder bumpers is also demonstrated.

4.2. Optimum bumper

The optimum bumper maximises the exposed solder protrusion available for plastic deformation within geometric constraints of the suspension system. For the model suspension in Fig. 2a, the distance between the opposing silicon bumpers is the limiting constraint. If the protrusion is too large, the opposing solder bumpers will combine upon reflow (Fig. 5). With a gap of just 192 µm between the silicon bumpers of the model suspension, the optimum conduit geometry has an opening width of 215 µm, creating a solder protrusion of approximately 80 µm (Fig. 4).

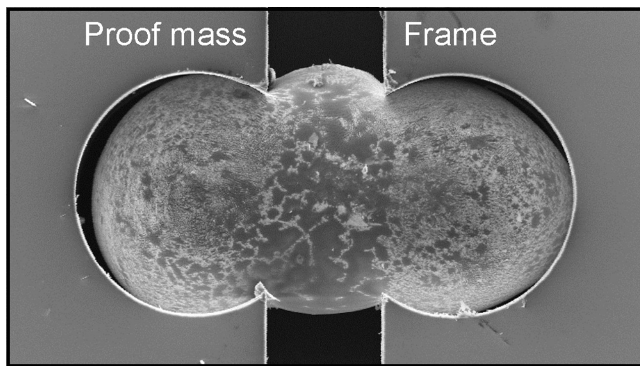

Fig. 5. Opposing solder bumpers combine upon reflow due to an excess of solder within the limited geometry.

5. Experimental

5.1. Experimental set-up

To investigate the protective ability of these bumpers, identical suspensions around proof mass ratios 1:2:4:6, with and without solder bumpers, were shock tested in a drop-test rig (Fig. 6). As a shock machine, a drop-test rig satisfied all of our requirements; it is relatively easy to manufacture and use, affordable to construct, can provide good repeatability and is capable of producing a directional shock of medium to high acceleration levels: 500–15,000g. Drop testing is also well established as a suitable method for shock testing MEMS sensors [10,21,22].

The basis of our drop-test rig is a solid base, a 2 m single guide rail and a carriage which is attached to the rail and holds the test sample. The bearing clearance of the carriage was carefully adjusted to find an optimum balance between friction (small clearance) and movement in unwanted directions (large clearance). To further minimise the effects of friction the guide rail is lubricated prior to every drop. A high-shock piezoelectric accelerometer (Kistler Type 8044) which can sense acceleration in the range of −20,000g to 30,000g is securely fastened to the carriage and records the deceleration value of each shock event. The accelerometer is connected to a charge amplifier (Kistler 5041E1) via a low noise cable (Kistler 1631C). The charge amplifier converts the electrical charge signal from the accelerometer to voltage, with a maximum voltage output of ±10 V. It is powered by a 24 V power supply, has a frequency range of 0–50 kHz and an adjustable capacitance range of 100–99,900 pC. This allows the amplifier to detect a wide range of accelerations. The output is sampled and converted from analogue to digital via a National Instruments NI USB-6210 data acquisition (DAQ) board which features a maximum sampling rate of 250 kHz. The resulting output is viewed in LabVIEW SignalExpress 2010.

5.2. Shock output

The magnitude of the shock pulse generated can be varied by altering the base or adjusting the drop height. An iron cuboid provides the solid base. The surface of the cuboid was polished to ensure perfect contact between the ground and cuboid to prevent resonance of the base upon impact of the falling carriage. M8 and M10 threaded holes were drilled into the cuboid, allowing rubber dampers of various sizes and shapes to be screwed into the base. Therefore the impact surface can be altered and thus the magnitude and the shape of the shock pulse greatly varied. For higher shocks, rubber sheets of varying thickness can be laid atop the iron cuboid.

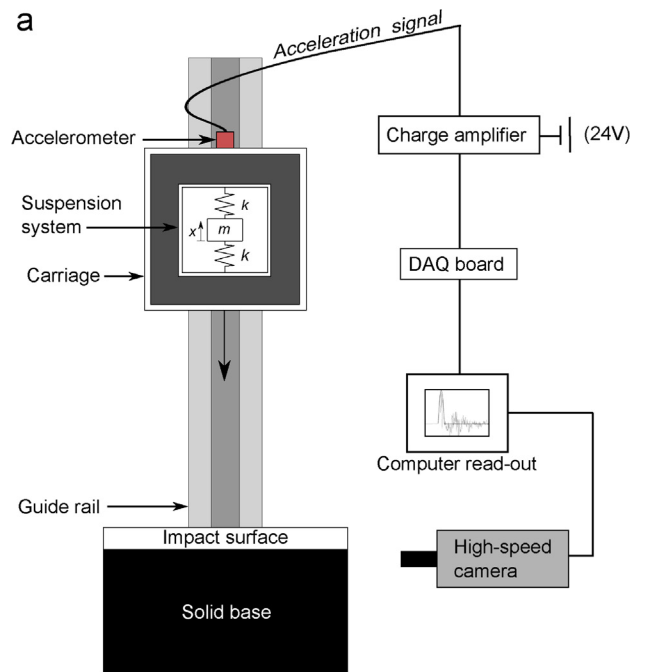

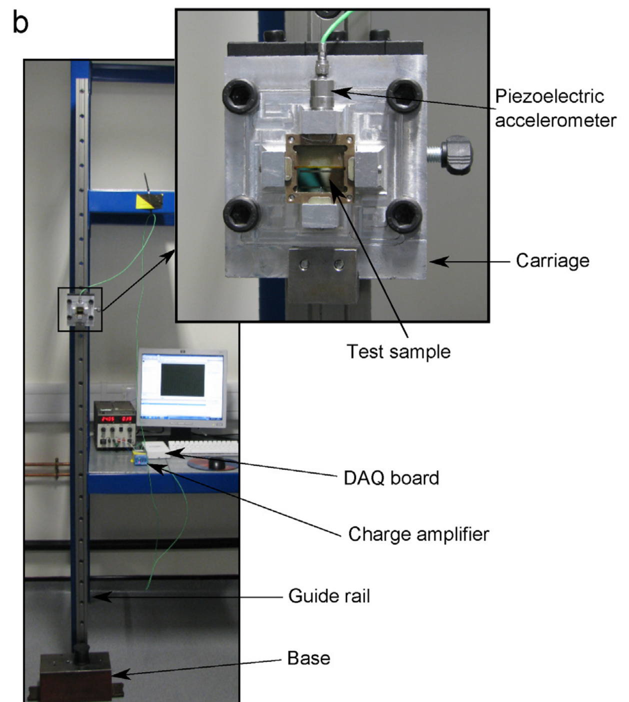

Fig. 6. (a) Our drop-test rig: schematic. The suspension system is modelled as single degree of freedom (SDOF) spring mass system. (b) Our drop-test rig, used for shock testing the MEMS suspension systems.

Fig. 7 shows an idealised half-sine wave superimposed upon a typical shock reading, generated when the carriage impacts a 1.5 mm rubber sheet atop the iron cuboid. This shock pulse ($a(t)$) excites the base of the suspension system during a shock event. For this set of experiments the shock range varied from 1000 to 6000g, of approximate half-sine duration of 200–300 μs.

5.3. High-speed photography

A Photron FASTCAM SA-3 (Monochrome) high-speed camera was used together with a high magnification lens and a 60 W

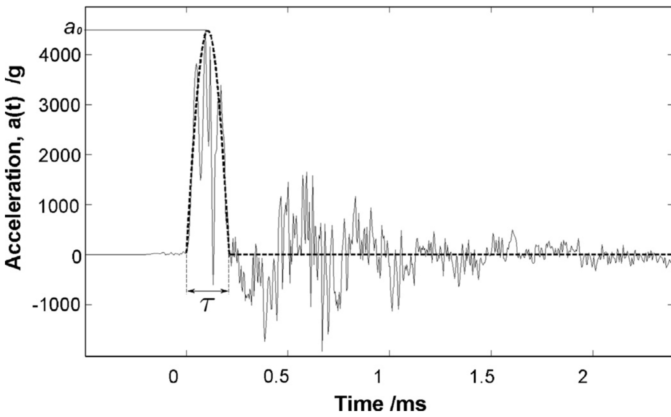

Fig. 7. Half-sine pulse superimposed on a typical shock reading.

metal halide light source to capture images of the suspensions and bumpers before, during and after the moment of impact at 100 μs intervals.

6. Results

6.1. Failure modes

A plot of the results for both unarmoured and armoured suspensions is shown in Fig. 8. Two failure modes were observed for the unarmoured suspensions: (1) failure shortly after impact due to fracture at the support of the lower cantilevers nearest the collision point; (2) later failure on rebound due to fractures at the folds of the upper cantilevers further from the impact point. No unarmoured suspension survived a shock greater than 2200*g*. For the armoured suspensions, failures only occurred during rebound (failure mode 2) with fractures at the folds of the upper cantilevers, and only at shocks above 4500*g*.

6.2. Failure probability

The results represented in Fig. 8 were fit with a Weibull shape distribution (Fig. 9), allowing the percentage of failures expected

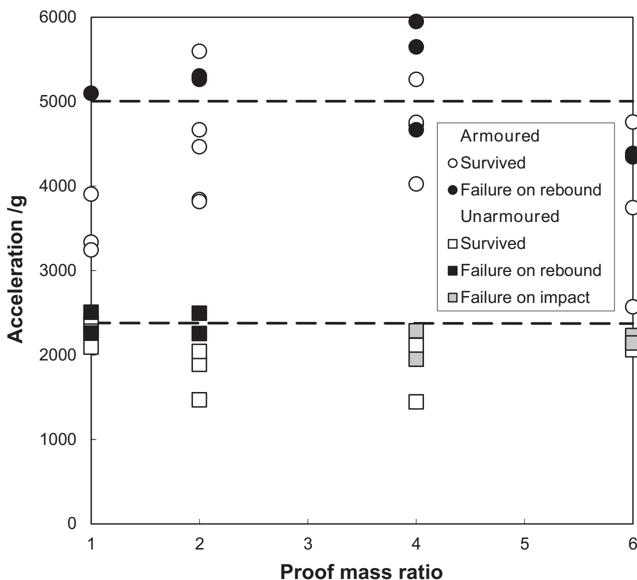

Fig. 8. Shock test results for the armoured and unarmoured suspensions. The threshold for the onset of failure on rebound is shown.

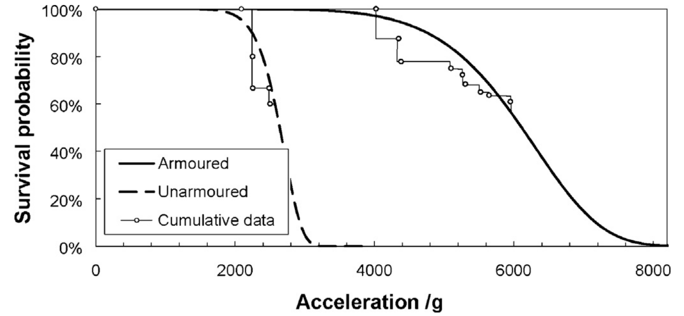

Fig. 9. Weibull plot for failure on rebound data. A cumulative plot of the failure data shows good correlation with the Weibull model.

at any given acceleration to be predicted. Failure on rebound alone was considered. Because the onset of failure appears to be independent of mass, the failure data for all the geometries was included in the plot. The characteristic life α, defined as the acceleration at which 63.21% of the population will fail and the Weibull modulus β were obtained to be 6419*g* and 8.1 respectively for the armoured suspensions and 3285*g* and 10.7 for the unarmoured suspensions, using a least squares fit. The comparable values of β indicate a similar failure rate and hence a similar failure mode whilst the characteristic life for the armoured devices is nearly twice that of the unarmoured equivalent, indicating that the provision of armouring doubled the shock resistance of the MEMS suspension.

6.3. Failure on impact

Failure on impact occurs if the initial impact force is large enough. It is the primary failure mode for the larger unarmoured geometries only. Failure occurs in the form of fractures at the collision point. Plastic deformation of the solder completely eliminates this failure mode for the armoured suspensions. Plastic deformation occurs only if the kinetic energy of the collision is large enough, in which case it is converted into plastic strain energy, elastic strain energy and elastic stress waves, plastic strain energy being by far the dominant mode of energy dissipation [23–27]. Fig. 10 shows the considerable energy absorbed at the bumpers by plastic deformation during a shock event of 5300*g* which the silicon suspensions survived.

6.4. Failure on rebound

Failures on rebound take the form of fractures at the folds of the upper cantilevers (Fig. 11d). High-speed microscopy shows that the upper springs resonate after collision with the rebounding proof mass (Fig. 11a–c). It is the closing velocity of this collision that determines the amplitude of the subsequent resonance of the springs [28].

7. Discussion

The suspension system is modelled as an undamped single-degree-of-freedom (SDOF) spring-mass system attached to an accelerating support (Fig. 6a); the equation of motion of the mass is given by (1), where ω_0 is the resonant frequency of the suspension:

$$\ddot{x} + \omega_0^2 x = a(t) \quad (1)$$

It is assumed that the interaction of the packaging with its environment determines the nature of the shock load transmitted to the suspension system [29]. The shock load is modelled as a

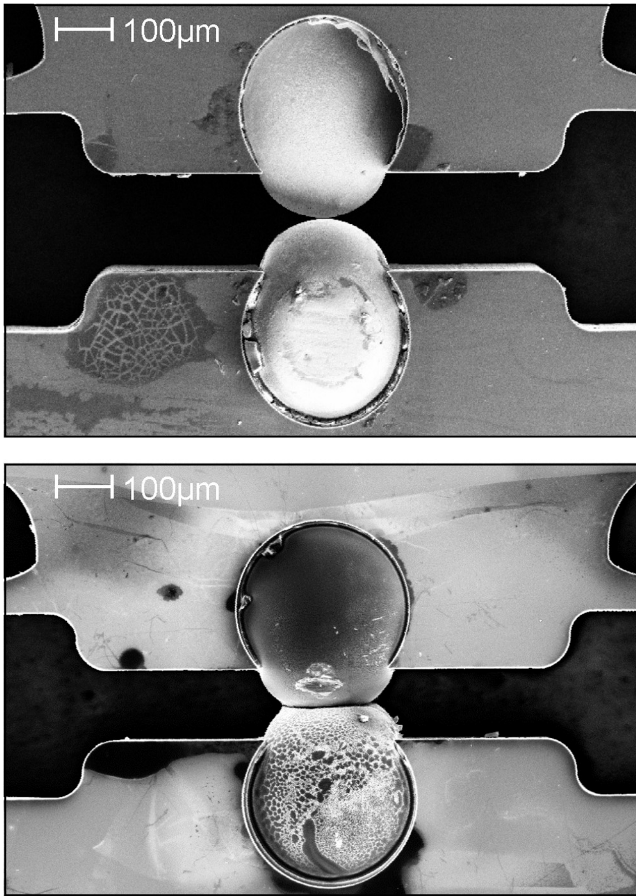

Fig. 10. Solder bumpers before and after impact exhibiting plastic deformation. The bumpers are adjacent to each other for the purpose of the image only. They remain separate and have not combined.

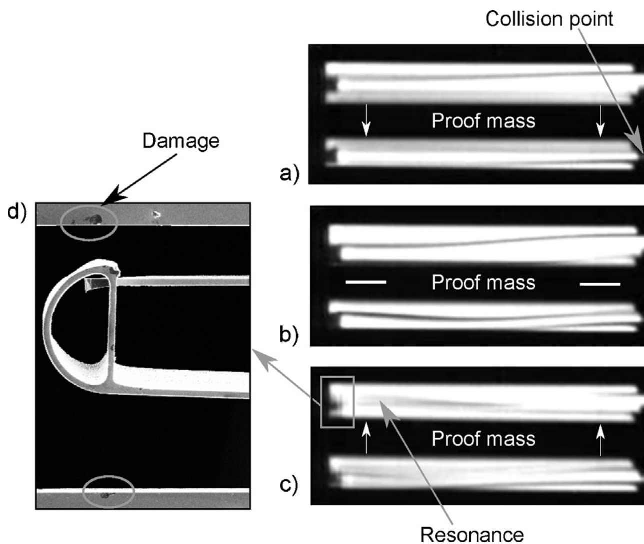

Fig. 11. High speed micrographs (10,000 fps): The left half of suspension system. (a) Prior to bumper collision the proof mass travels downwards, (b) the instant of the collision between the lower bumpers, (c) the proof mass rebounds and strikes the upper springs into resonance, as evident from the motion blurring, and (d) micrograph of upper spring damage, highlighting collision damage.

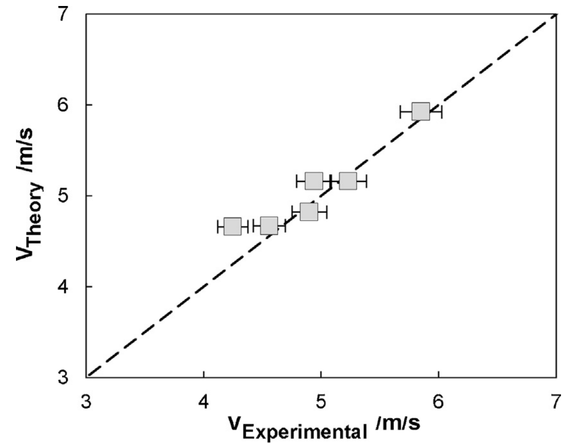

Fig. 12. Experimental and theoretical velocities are compared, the dashed line represents $V_{Theory} = V_{Experimental}$. Error bars accounting for motion blurring in the high-speed micrographs are included.

half-sine wave (Fig. 7); expressed mathematically as (2), where a_0 is the amplitude and τ is the duration:

$$a(t) = \begin{cases} a_0 \quad \sin\left(\frac{\pi t}{\tau}\right), & 0 \le t \le \tau \\ 0, & t \ge \tau \end{cases} \tag{2}$$

There are two impacts to consider when analysing the response of the system: the external impact which determines the amplitude and duration of the shock pulse $a(t)$ applied to the outer frame; and the internal collision between the bumpers, determined by the response of the proof mass to the external impact. This internal response is dependent on the duration of the external shock pulse with respect the natural period of the suspension.

Following Ayre [30], if the duration of the applied pulse is short relative to the natural period (T), to be precise if $\tau < T/4$, the response of the suspension can be obtained by equating the impulse of the external shock to the change in momentum of the proof mass, i.e. the response is identical to an unforced system with proof mass velocity just after impact, with respect to the frame given by the integral of the acceleration pulse [29]:

$$\dot{x}_0 = \left(\int_0^{\tau} a(t)dt\right) = \frac{2a_0\tau}{\pi} \tag{3}$$

For the measured resonant frequencies of our structures, the shock pulse is considerably less than one quarter of the period. Therefore whilst it is expected that the impact force will be mass dependent, it is clear that the velocity (defined by Eq. (3)) is not. High-speed micrographs were used to verify that the proof mass velocity prior to the moment of collision is approximately equal to (3) (Fig. 12).

Fig. 8 suggests that the onset of failure on rebound for both the unarmoured and armoured suspensions is not strongly dependent on mass. To quantify a power law of m^p fitted to the data gives exponents of -0.04 ± 0.09 and -0.07 ± 0.07 respectively, indistinguishable from $p = 0$ and hence is consistent with the collision velocity, rather than the size of the proof mass determining the threshold for failure.

High-speed micrographs were also used to establish the coefficient of restitution of both silicon and solder. The rebound velocity of the proof mass, which determines the closing velocity of the collision between the proof mass and upper spring is equal to the coefficient of restitution multiplied by the initial proof mass velocity (3). The ratio of the velocities before and after collision give

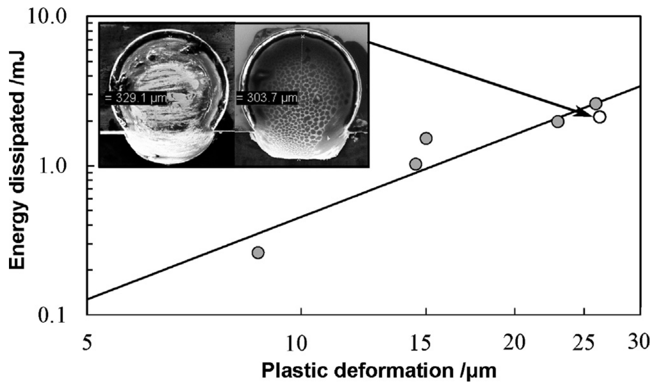

Fig. 13. Energy dissipated by the solder bumpers during the initial lower bumper impact plotted as a function of plastic deformation on a log–log scale. SEM images were used to measure the depth of plastic deformation.

approximate coefficients of restitution of $e_{si} = 0.75$ for the silicon and $e_{solder} = 0.36$ for the solder, in agreement with published values [9]. The solder gives a reduction of 2.08 in the collision velocity, compared to the observed 2.1 increase in the shock level for failure. It is this reduction in the collision velocity due to inelastic deformation that has increased the robustness.

8. Energy dissipated

8.1. Plastic deformation

To quantify the energy dissipated by the solder through plastic deformation, the kinetic energy lost during the initial lower bumper impact (estimated using high-speed micrographs) is plotted as function of plastic deformation in Fig. 13.

During compression the energy of the impact is transformed into the internal energy of deformation by a contact force (F_c). This contact force is a reaction force that resists deformation, it acts equally on each colliding body (i.e. on each bumper) but in opposite directions. F_c increases with increasing deformation and reduces the relative velocity between the two bumpers. Compression terminates when the relative velocity between the two bumpers is zero [31]. The work done (W) or energy dissipated by the bumpers can be related to the contact force by (4), where δ is the depth of plastic deformation:

$$W = \int_0^{\delta} F_c d\delta \quad (4)$$

Fig. 14 plots plastic deformation versus the contact force for a single solder bumper on a *log–log scale*, the area under this

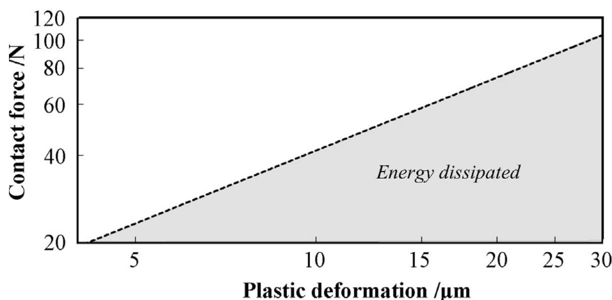

Fig. 14. The contact force between the two colliding solder bumpers plotted as a function of plastic deformation on a log–log scale. The area under the graph corresponds to the energy dissipated by one solder bumper.

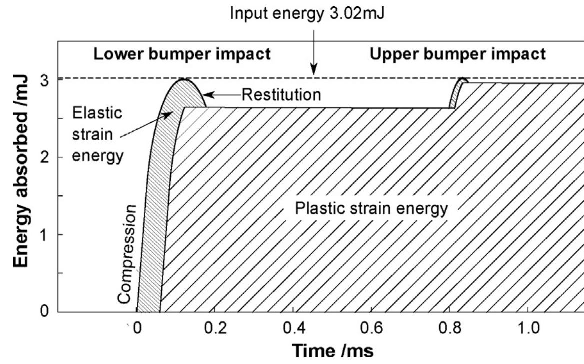

Fig. 15. Proof mass energy partition during drop testing. High-speed micrographs were used to estimate the timings between bumper collisions and to verify that the initial bumper impact absorbs the majority of the kinetic energy, and the subsequent upper bumper impact brings the proof mass nearly to a rest. Durations for compression and restitution are exaggerated and indicative only.

force–displacement curve is the work done or energy dissipated by one solder bumper.

8.2. Total energy dissipated

During impact the majority of the energy of the system is converted into plastic strain energy, energy dissipated by elastic stress waves will be negligible in comparison [23–27]. Fig. 15 shows the energy partition of the proof mass belonging to the suspension system highlighted in Fig. 13. During the initial impact the bumpers on the lower side of the proof mass plastically deform, absorbing the majority of the energy, with the proof mass coming fully to rest when the contact force is at its maximum; at this point the kinetic energy of the proof mass is zero. During the restitution stage, the elastic strain energy stored in the system during compression generates a force that drives the two bumpers apart with a relative velocity equal to the impact velocity times the coefficient of restitution, this rebound energy is equal to the elastic strain energy stored during compression. The majority of the remaining energy is dissipated when the upper bumpers collide.

9. Conclusion

Solder armouring has proved to be an extremely effective shock absorber for MEMS suspensions. A significant fraction of the kinetic energy (in this case $1 - e_{solder}^2 \approx 0.9$) of a shock event is absorbed through plastic deformation of the solder bumpers during the initial collision within the MEMS suspension. Readily incorporated into current fabrication methods the solder bumpers remove failure on impact and in this case have doubled robustness to damage on rebound.

Acknowledgments

The authors are grateful to the UK Space Agency for financial support as part of the development of a microseismometer for the InSight mission to Mars and the EPSRC engineering instrument pool for the loan of the high speed photography equipment.

References

[1] T.G. Brown, B. Davis, D. Hepner, J. Faust, C. Myers, C. Muller, et al., Strap-down microelectromechanical (MEMS) sensors for high-g munition applications, IEEE Transactions on Magnetics 37 (2001) 336–342.
[2] H. Shea, Reliability of MEMS for space applications, in: Photonics West 2006: Reliability, Packaging, Testing, and Characterization of MEMS/MOEMS V, San Jose, CA, USA, 2006.

[3] R.R.A. Syms, Scalable electrothermal MEMS actuator for optical fibre alignment, Journal of Micromechanics and Microengineering 14 (2004) 1633–1639.
[4] F.T. Hartley, Micropump technology and applications, in: SPIE Conference on Electronics and Structures for MEMS, Qld, Australia, 1999, pp. 403–409.
[5] K. Ikuta, S. Aritomi, T. Kabashima, Tiny silent linear cybernetic actuator driven by piezoelectric device with electromagnetic clamp, in: Micro Electro Mechanical Systems, 1992, MEMS'92, Proceedings. An Investigation of Micro Structures, Sensors, Actuators, Machines and Robot. IEEE, 1992, pp. 232–237.
[6] T. Hopf, S. Kumar, W.J. Karl, W.T. Pike, Shock protection of penetrator-based instrumentation via a sublimation approach, Advances in Space Research 45 (2010) 460–467.
[7] D.M. Tanner, J.A. Walraven, K. Helgesen, L.W. Irwin, F. Brown, N.F. Smith, et al., MEMS reliability in shock environments, in: Reliability Physics Symposium, 2000, Proceedings. 38th Annual 2000 IEEE International, 2000, pp. 129–138.
[8] D. Jordy, M.I. Younis, Characterization of the dynamical response of a micromachined G-sensor to mechanical shock loading, Journal of Dynamic Systems, Measurement, and Control 130 (2008) 41003.
[9] S.W. Yoon, N. Yazdi, N.C. Perkins, K. Najafi, Micromachined integrated shock protection for MEMS, Sensors and Actuators A: Physical 130–131 (2006) 166–175.
[10] S.W. Yoon, S. Lee, N.C. Perkins, K. Najafi, Shock-protection improvement using integrated novel shock-protection technologies, Journal of Microelectromechanical Systems 20 (2011) 1016–1031.
[11] H. Shusen, L. Xinxin, W. Yuelin, J. Jiwei, G. Xiaohong, L. Deren, et al., A piezoresistive accelerometer with axially stressed tiny beams for both much increased sensitivity and much broadened frequency bandwidth, in: TRANSDUCERS, 12th International Conference on Solid-State Sensors, Actuators and Microsystems, vol. 1, 2003, pp. 91–94.
[12] S.-H. Yoon, Woodpecker-inspired shock isolation by microgranular bed, Journal of Physics D: Applied Physics 42 (2009) 35501.
[13] M.A. Macauley, Introduction to Impact Engineering, Chapman and Hall, London/New York, 1987.
[14] A. Delahunty, W.T. Pike, Integrating solder bumpers for high shock applications, in: 2013 IEEE 26th International Conference on Micro Electro Mechanical Systems (MEMS), 2013, pp. 689–692.
[15] W.T. Pike, W.J. Karl, S. Kumar, S. Vijendran, T. Semple, Analysis of sidewall quality in through-wafer deep reactive-ion etching, Microelectronic Engineering 73–74 (2004) 340–345.
[16] R. Khanna, Microfabrication protocols for deep reactive ion etching and wafer-level bonding, Sensors 18 (2001) 51–60.
[17] C.J. Mogab, The loading effect in plasma etching, Journal of The Electrochemical Society 124 (1977) 1262–1268.
[18] J.W. Coburn, H.F. Winters, Conductance considerations in the reactive ion etching of high aspect ratio features, Applied Physics Letters 55 (1989) 2730–2732.
[19] S. Kumar, W.T. Pike, Technique for eliminating notching in through-wafer etching, in: 16th MME Micromechanics Europe Workshop, Goteburg, Sweden, 2005, pp. 88–91.
[20] K. Brakke, Surface Evolver Documentation, 2007.
[21] S. Mariani, A. Ghisi, A. Corigliano, S. Zerbini, Multi-scale analysis of MEMS sensors subject to drop impacts, Sensors 7 (2007) 1817–1833.
[22] L. Jing-en, T. Tong Yan, Z. Xueren, E. Hussa, W. Jason, C. Ford, et al., Drop impact life prediction models with solder joint failure modes and mechanisms, in: Electronic Packaging Technology Conference, 2005. Proceedings of 7th EPTC 2005, 2005, 7 pp.
[23] I.M. Hutchings, Energy absorbed by elastic waves during plastic impact, Journal of Physics D: Applied Physics 12 (2001) (1819).
[24] F. Li, J. Pan, C. Sinka, Contact laws between solid particles, Journal of the Mechanics and Physics of Solids 57 (2009) 1194–1208.
[25] C.Y. Wu, L.Y. Li, C. Thornton, Energy dissipation during normal impact of elastic and elastic–plastic spheres, International Journal of Impact Engineering. 32 (2005) 593–604.
[26] C. Wu, L. Li, C. Thornton, Rebound behaviour of spheres for plastic impacts, International Journal of Impact Engineering. 28 (2003) 929–946.
[27] L.Y. Li, C.Y. Wu, C. Thornton, A theoretical model for the contact of elastoplastic bodies, Proceedings of the Institution of Mechanical Engineers, Part C: Journal of Mechanical Engineering Science 216 (2002) 421–431.
[28] S. Rubin, Concepts in shock data analysis, in: Shock and Vibration Handbook, 5th ed., McGraw-Hill, New York, 2002.
[29] V.T. Srikar, S.D. Senturia, The reliability of microelectromechanical systems (MEMS) in shock environments, Journal of Microelectromechanical Systems 11 (2002) 206–214.
[30] R.S. Ayre, Transient response to step and pulse functions, in: Shock and Vibration Handbook, 5th ed., McGraw-Hill, New York, 2002.
[31] W.J. Stronge, Impact Mechanics, Cambridge University Press, Cambridge, 2000.